Insights into the functionalities of cellulose acetate and microcrystalline cellulose on water absorption, crystallization, and thermal degradation kinetics of a ternary polybutylene succinate-based hybrid composite

Thomas Sango, Ahmed Koubaa, Mohamed Ragoubi, Martin Claude Ngueho Yemele, Nathalie Leblanc

▶ To cite this version:

Thomas Sango, Ahmed Koubaa, Mohamed Ragoubi, Martin Claude Ngueho Yemele, Nathalie Leblanc. Insights into the functionalities of cellulose acetate and microcrystalline cellulose on water absorption, crystallization, and thermal degradation kinetics of a ternary polybutylene succinate-based hybrid composite. Industrial Crops and Products, 2024, 222, pp.119572. ⟨10.1016/j.indcrop.2024.119572⟩. ⟨hal-04840799⟩

HAL Id: hal-04840799
https://normandie-univ.hal.science/hal-04840799v1

Submitted on 16 Dec 2024

Industrial Crops & Products 222 (2024) 119572

Contents lists available at ScienceDirect

Industrial Crops & Products

journal homepage: www.elsevier.com/locate/indcrop

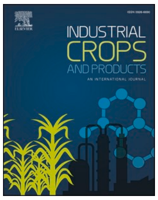

Insights into the functionalities of cellulose acetate and microcrystalline cellulose on water absorption, crystallization, and thermal degradation kinetics of a ternary polybutylene succinate-based hybrid composite

Thomas Sango [a,b], Ahmed Koubaa [a,*], Mohamed Ragoubi [b], Martin Claude Ngueho Yemele [c], Nathalie Leblanc [b]

[a] *Forest Research Institue (Institut de recherche sur les forêts–IRF), University of Québec in Abitibi–Témiscamingue (UQAT), 445 Boul. de l'Université, Rouyn-Noranda, QC J9X 5E4, Canada*
[b] *UniLaSalle, Unité de recherche Transformations & Agro-Ressources, VAM^{2}IN (EA 7519 UniLaSalle-Université d'Artois), Mont Saint Aignan, France*
[c] *Natural Resources Canada, Natural Climate Solutions Division, 580 Booth St, Ottawa, ON K1A 0E4, Canada*

ARTICLE INFO

Keywords:
Polybutylene succinate
Cellulose acetate
Microcrystalline cellulose
Polymer blends and Hybrid composites
Nucleation and crystallization
Thermal degradation

ABSTRACT

The kinetic behavior of a polymer material filled with natural and/or functionalized reinforcement can evolve regarding water absorption, crystallization, and thermal degradation (TD) processes. This study investigates the separate and combined influence of microcrystalline cellulose (MCC) and cellulose acetate (CA) on changes in the water absorption percentage (WAP), crystallization, and TD kinetics of polybutylene succinate (PBS) based materials. Disc-shaped neat PBS (n-PBS), binary (PBS/CA, PBS/MCC), and ternary hybrid (PBS/CA/MCC) specimens were produced via extrusion and injection. SEM observations of the hybrid micrographs revealed that MCC was whitish-coated by a CA layer that forms an "amphiphilic"-like co-continuous interphase between PBS and fibers. The CA encapsulation activity limited the hybrid's WAP in the first week of water conditioning tests. In contrast, in the second immersion period, the WAP was increased by 19 % compared to that for PBS/MCC due to the synergistic activities of plasticized fillers. Avrami outcomes at 80°C showed that the hybrid's half-crystallization time ($t_{0.5}$) increased by 64 % and 104 % compared to n-PBS and PBS/MCC, respectively, indicating that the enrobing CA layer restrained the slight nucleating effect of MCC fibers. The hybrid activation energy (E_a) values determined at lower conversion rates ($\alpha \leq 0.25$) following the Flynn–Wall–Ozawa (F–W–O) model showed that they were up to 14 % higher than those for PBS/MCC, evidencing that CA delayed the TD of MCC fibers. For higher conversion rates ($\alpha \geq 0.5$), the synergy of both fillers postponed the TD of PBS. The E_a values obtained from the Kissinger method confirmed previous findings.

1. Introduction

Cellulose $[(C_{12}H_{20}O_{10})_n]$ is well-known as the most abundant sustainable biosourced polymer on Earth (Azman Mohammad Taib et al., 2022). It is a linear homopolysaccharide of biological origin whose repeating unit is cellobiose, a dimer of β-(1→4) linked D-glucopyranose units. The glucose ring contains three hydroxyl functions (HO −), at C_2, C_3, C_6 positions which are responsible for the dimensional instability and chemical reactivity of cellulose (Azman Mohammad Taib et al., 2022). Although cellulose has satisfactory nucleating efficiencies in thermoplastic polymers, it is less thermally stable than cellulose acetate (CA) because it starts degrading at ~230°C (Huang et al., 2017; Ku et al., 2011). CA is the simpler and most common ester derivative of cellulose (Boulven et al., 2019). It is obtained through esterification, i.e., chemical substitution of −OH groups of cellulose backbones with acetate functions (Boulven et al., 2019; Huang et al., 2017). In its poly-acetylated state, CA can be used as a matrix ingredient to produce fully biobased composite materials with cellulose fibers as reinforcement (Boulven et al., 2019). Unfortunately, CA chain structures contain residual HO − that can interact through hydrogen bonds (H-bonds) and rigid cyclic D-glucopyranose segments that restrain the mobility of CA macromolecules at room temperature (R.T. – 25°C). These structural configurations explain the brittleness of the biosourced material. Even though CA plasticizes significantly at high acetylation degrees – the acetylation

---

* Corresponding author.
E-mail address: ahmed.koubaa@uqat.ca (A. Koubaa).

https://doi.org/10.1016/j.indcrop.2024.119572
Received 7 April 2024; Received in revised form 6 August 2024; Accepted 29 August 2024
Available online 4 September 2024

degree is also referred as the Degree of Substitution – (DS≥2.45), its glass transition temperature (T_g) remains high, such that CA is relatively unmalleable without additional pre-treatment (Quintana et al., 2013). Note that the DS is the average number of HO – substituted by acetate groups per anhydroglucose (AGU) unit.

Therefore, before being incorporated into a blend, CA generally requires pre-treatment with a substantial amount of external plasticizers (~ 30 wt%) (Pang et al., 2015). These additives are small molecules (e.g.: xylitol, glycerol, polyethylene glycol, triethyl-citrate, phthalate esters) that can either volatilize or migrate towards the surroundings of materials that are prone to compromise their initial properties (Quintana et al., 2013), resulting in weaker performance, accelerated material aging, and negative effects on human health and the environment (Boulven et al., 2019). Highly ductile bio-polyesters (e.g.: polybutylene adipate terephthalate–PBAT, polycaprolactone–PCL, PBS) have been reported as softenibility enhancers of brittle polymers such as polylactic acid–PLA and polyhydroxyalkanoates–PHAs (Aliotta et al., 2022; Barletta et al., 2022; Platnieks et al., 2021a; Rafiqah et al., 2021; Zhang et al., 2021). Hence, instead of external plasticizers, PBS can be mixed with CA to yield a potentially softer and more malleable blend, depending on the quantities of the components (Aliotta et al., 2022).

PBS is a semi-crystalline thermoplastic biopolyester with excellent processability, good thermal stability, and broad interest for applications such as packaging and automotive industries, among others (Barletta et al., 2022; Rafiqah et al., 2021). This fully compostable aliphatic polymer contains highly flexible macromolecules thanks to its relatively low PBS T_g (between −40 and −10°C) (Platnieks et al., 2021a). It is suitable for improving the softenibility and malleability of brittle CA/MCC brittle blends (Platnieks et al., 2021b). Several studies have reported outstanding results on the evolution of the water absorption percentage (WAP), crystallization, and TD kinetics in binary and ternary hybrid composites made with a matrix of one or two thermoplastic biopolyesters (PBS, PBAT, PLA) blended with natural or functionalized polysaccharide reinforcements (Barletta et al., 2022; Hu et al., 2017; Li et al., 2017; Monika et al., 2019; Vorawongsagul et al., 2021; Zhang et al., 2021, 2018; Zhang and Wang, 2018; Zhou et al., 2016). However, no study to date has investigated the evolution of WAP, crystallization, and TD kinetics in a ternary hybrid composite with PBS/CA as a co-matrix reinforced with MCC fibers.

Nowadays, polysaccharide-reinforced thermoplastic composites are used for rigid packaging, luxury decoration, and automotive applications under peculiar environmental situations (Aliotta et al., 2022; Barletta et al., 2022; Zhang et al., 2021). For example, when exposed to heat or humidity, the behavior of cellulose-filled polyester materials can evolve during the service period. Therefore, from both academic and industrial perspectives, it is important to study the influence of both fillers (CA and MCC) on the WAP of PBS-based blends in order to understand, control and optimize industrial processes. The relative resilience of CA and MCC fibers to ambient conditions (such as heat and water molecules in the humidity) can affect the microstructure (degree of crystallinity and morphology) of a multiphase PBS-based composite, and hence its final performance (Ahmad Thirmizir et al., 2011; Zhang et al., 2018, 2021). Several investigations have shown that adding CA or MCC to PBS influences the evolution of the WAP and diffusivity in the resulting binary blends, both parameter values increasing with increasing filler content (Čîhal et al., 2018; Espert et al., 2004; Frollini et al., 2013; Zhang et al., 2018, 2021).

Furthermore, it has already been proved that the addition of the CA to the PBS gradually reduces the crystallization rate (CR) of the PBS/CA blend compared to the neat PBS (Čîhal et al., 2018; Shi et al., 2018). Hu et al. (2017) demonstrated that, even at high cellulose fiber loadings (40 wt%), MCC slightly increased the nucleation density (and thus the CR) of PBS/MCC composites. In a context where MCC fibers are mixed with a miscible blend of PBS and CA, would there be either a synergistic or an interference effect of the combined fillers on the crystallization kinetics of the PBS/CA/MCC?

The TD behavior of a polymer-based composite is generally affected by the content of the polysaccharide-sourced fillers (Sun, et al., 2016; Zhang et al., 2020) due to their low thermal stability compared to that of pure polymer. Furthermore, by determining the E_a, it is possible to comprehend the complexities behind the TD mechanisms (Mothé and de Miranda, 2013; Zanatta et al., 2016). The F–W–O and Kissinger approaches are popular isoconversional models for estimating the E_a of thermally stimulated processes studied by DTG (Monika et al., 2019; Mothé and de Miranda, 2013; Sun, et al., 2016; Wellen and Canedo, 2014).

The particularity of the present study lies in its exploration of the separate and combined influences of CA and MCC on the evolution of the WAP, crystallization, and TD kinetics in a ternary PBS-based hybrid composite. PBS, CA, and MCC were blended using the twin-screw extrusion, and specimens (n-PBS, PBS/CA, PBS/MCC, and PBS/CA/MCC) were fabricated via injection molding. SEM, gravimetric measurements, DSC, and TGA-DTG analysis were used to monitor changes.

2. Experimental section and theory

2.1. Materials

Cellulose acetate (CA) flour – CAS number: 9035–69–2 – with an acetyl content of 39 %, i.e., a DS of 2.45, and molecular mass (M_n) of 30 000 g.mol^{-1} was purchased from Sigma Aldrich. PBS pellets with a density of 1.26 g.mL^{-1} and a mass flow index (MFI) of 4–7 g/10 min (190°C, 2.16 kg) were acquired from Shijiazhuang Tuya Technology Company (China) under the product code TH803S. MCC (130 µm, aspect ratio L/D of 2.2) fibers were provided by Josef O. Rettenmaier (Fosston, USA).

2.2. Preparation of PBS-based materials

PBS and CA were oven-dried at 70°C for 24 h before extrusion. MCC was oven-dried at 103°C overnight. The studied formulations are summarized in Table 1.

PBS-based materials were prepared following several steps in order to identify the single and combined influence of both fillers on the PBS backbone. Corresponding amounts of PBS and CA were extruded together at a speed of 50 rpm using a counter-rotating twin-screw extruder (HAAKE Polylab OS Rheodrive 7, HAKKE, Karlsruhe, Germany) following the temperatures profile of 120–180–225–120°C. This first extrusion step made it possible to melt completely CA crystals at 225°C.

The extrusion line used in this study is divided in 4 sections: many temperature conditions were tested and the optimized profile 120–180–225–120°C was adopted. CA particles and PBS pellets melt at 225°C and ~117°C, respectively. The ternary hybrid composite studied here was prepared in particular way:

- the temperature of the first section was set at 120°C because PBS pellets started to melt at that temperature. This helped to start “plasticizing” CA particles.
- the temperature of the second section was set at 180°C. At that temperature, PBS pellets are already melted and CA particles are sufficiently “plasticized”. At this step, the crystallites of CA are not yet melted;

Table 1
PBS-based specimen formulations and codes.

Formulations	Ingredients		
	PBS (wt%)	CA (wt%)	MCC (wt%)
n-PBS	100	—–	—–
PBS/CA	80	20	—–
PBS/MCC	70	—–	30
PBS/CA/MCC	50	20	30

- at 225°C, CA particles were melted with the aim to produce the PBS/CA binary co-matrix. At this temperature, the mobility of PBS chains is very high. This facilitated the dispersion of melted CA macromolecules. If CA had not been processed as previously described, it would have acted as a reinforcing element with MCC fibers. This was not the targeted objective: the goal is to prepare a hybrid matrix composite instead of a hybrid reinforcement composite.
- the temperature of the fourth zone (120°C) was reduced in order to recover the polymer filament.

The resulting extruded particles were then mixed with the corresponding amount of MCC using a Haake (HAAKE Rheomix, Karlsruhe, Germany) compounder and extruded again at another temperatures profile (120–140–160–120°C). From author's point of view, since CA particles were already melted, it was not necessary to keep the first temperatures profile. It is noteworthy to mention that the second profile was also optimized. The maximum temperature in this step is 160°C which is lower to the onset degradation temperature of MCC fibers (~200°C). This helped to extrude the composites without altering the fibers microstructure. Disc-shaped specimens were produced using injection molding (MARS II130/600, Haitian, Ningbo, China) at barrel temperatures ranging from 140 to 170°C. As described earlier, the extrusion and injection processes have been thoroughly optimized in order to produce less defected materials.

2.3. *Characterization of PBS-based materials*

2.3.1. *Water absorption measurements*

Water absorption (WA) measurements were conducted by direct immersion of n-PBS and PBS-based blends in distilled water at ambient temperature according to ASTM D570–81 standard. Specimens were oven-dried at 70°C for 12 h, cooled, and immediately weighed to the nearest 0.001 g. The specimens were then immersed in distilled water for 125 days at R.T. After 8 days of conditioning, they were removed from water. Any surface water was blotted off with paper towels and the specimens were weighed immediately to the nearest 0.001 g and re-immersed in the water. The percentage of weight increased due to WA was calculated to the nearest 0.01 % according to Eq. (1):

$$\%(\mathbf{W_a}) = \frac{\mathbf{W_d} - \mathbf{W_0}}{\mathbf{W_0}} \times \mathbf{100} \tag{1}$$

where $\mathbf{W_a}$ is the total mass of absorbed water, $\mathbf{W_d}$ is the mass of the specimen after 8 days of immersion, and $\mathbf{W_0}$ is the initial specimen mass. All values were averaged from three replicates.

Gravimetric measurements of the WA kinetics of PBS-based blends were carried out following Fick's law of mass transport. The absorption mechanisms can be determined by performing the WA kinetics and fitting the experimental data of Eq. (2):

$$\frac{\mathbf{W_a}}{\mathbf{W_e}} = \mathbf{kt^n} \tag{2}$$

Eq. (2) can be rewritten in logarithmic form as Eq. (3):

$$\log\frac{\mathbf{W_a}}{\mathbf{W_e}} = \log\boldsymbol{k} + \mathbf{n}\log\mathbf{t} \tag{3}$$

where $\mathbf{W_e}$ is the maximum amount of water absorbed at the equilibrium state. The constants $\boldsymbol{k}$ and $\boldsymbol{n}$ can be determined from the slope and intercept of the curve plotting $\log(\frac{\mathbf{W_a}}{\mathbf{W_e}})$ versus $\log\mathbf{t}$. The constant values depend on the absorption mechanisms: for Fickian diffusion, $n = 0.5$; for pseudo-Fickian, $n < 0.5$; for relaxation-controlled, $n > 0.5$; and for anomalous transport (non-Fickian), $0.5 < n < 1.0$ (Petchwattana et al., 2017). WA in natural fiber-reinforced polymer materials generally exhibits Fickian diffusion behavior because the $\boldsymbol{n}$ values are similar and close to 0.5 for all specimens (Espert et al., 2004).

The next step was to analyze the parameters of the theoretical model. The diffusion coefficient $\boldsymbol{D}$ is the most important parameter of Fick's model, as it represents the ability of the swelling liquid to diffuse within the material structure. For short times ($\frac{\mathbf{W_a}}{\mathbf{W_e}} \leq \mathbf{0.5}$), Eq. (4) can be used to estimate $\boldsymbol{D}$ (Petchwattana et al., 2017).

$$\frac{\mathbf{W_a}}{\mathbf{W_e}} = \frac{4}{l}\left(\frac{D}{\pi}\right)^{1/2} t^{1/2} \tag{4}$$

where $\boldsymbol{l}$ is the thickness of the specimen. The $\boldsymbol{D}$ values were determined from the slope of the linear part of the plot of $\frac{\mathbf{W_a}}{\mathbf{W_e}}$ versus $t^{1/2}$.

2.3.2. *Non-isothermal DSC measurements*

Non-isothermal calorimetric measurements of n-PBS and its blends were performed using a DSC Q20 calorimeter (TA Instruments, USA) under dry nitrogen (N_2) flow. Temperature and energy calibrations were performed using pure zinc and indium. Specimens (10–20 mg) were placed in an aluminum pan and scanned from 20 to 180°C at a heating rate of 50°C.min^{-1}, held at 180°C for 5 min to erase the previous thermal history, and cooled at 20°C at a cooling rate of 10°C.min^{-1}. The crystalline weight fractions were computed from the enthalpy of the crystallization exotherms using Eq. (5):

$$\chi_{\mathrm{hc}} = \frac{\boldsymbol{\Delta H_{hC}}}{\boldsymbol{w\Delta H_m^0}} \times \mathbf{100} \tag{5}$$

where $\Delta H_m^0 = 110.3$ J/g (Hu et al., 2017) is the standard melting enthalpy corresponding to an infinitely thick perfect PBS α–crystals, and $\boldsymbol{w}$ is the mass fraction of the PBS in the formulation. The hot crystallization enthalpy ($\Delta \mathrm{H_{hc}}$) values were computed by integrating the exothermic peaks on the cooling curves between 80 and 140°C.

2.3.3. *Isothermal DSC measurements*

Isothermal DSC measurements of n-PBS and PBS-based blends were investigated using the same DSC Q20 calorimeter under N_2 flow. Specimens were scanned separately from 20 to 180°C at a heating speed of 50°C.min^{-1} and then maintained at 180°C for 5 min to fully melt the materials. Specimens were then quenched at selected temperatures (60, 75, 80, 85, and 90°C) for 50 min to enable crystallization. Specimens were then rapidly cooled to 20°C at 50°C.min^{-1}. From the thermograms, the heat of crystallization at time t ($\Delta \mathrm{H_t}$) and the related degree of crystallinity within the PBS fraction (χ_t) were determined. Note that $\mathrm{T_C}$, $\Delta \mathrm{H_t}$, and χ_t were determined from the cooling scan. The relative crystallization degrees (χ_t) were computed from the crystallization exothermic enthalpy using Eq. (6):

$$\chi_t = \frac{\boldsymbol{\Delta H_t}}{\boldsymbol{w\Delta H_m}} = \frac{\int_0^t \left(\frac{dH}{dt}\right) \boldsymbol{dt}}{\boldsymbol{w}\int_0^\infty \left(\frac{dH}{dt}\right) \boldsymbol{dt}} \tag{6}$$

where ΔH_m is the maximum crystallization enthalpy and $\mathbf{w}$ is the mass fraction of PBS in the formulation.

The isothermal crystallization kinetics of the PBS-based materials were investigated at $\mathrm{T_C}$ ranging from 60 to 90°C using the Avrami equation Eq. (7):

$$1 - \boldsymbol{\chi_t} = \exp(-\boldsymbol{kt^n}) \tag{7}$$

where $\boldsymbol{\chi_t}$ represents the relative crystallinity degree at crystallization time t. The parameters $\boldsymbol{n}$ and $\boldsymbol{k}$ are the Avrami exponent and the crystallization constant, respectively. They are related to the nucleation process and crystal geometry. Eq. (7) can be rearranged into the following logarithmic form as Eq. (8):

$$\ln[-\ln(1-\boldsymbol{\chi_t})] = \ln\boldsymbol{k} + \boldsymbol{n}\ln\boldsymbol{t} \tag{8}$$

By plotting the line of $\ln[-\ln(1-\boldsymbol{\chi_t})]$ versus $\ln\boldsymbol{t}$, the values of slope $\boldsymbol{n}$ and the intercept $\ln\boldsymbol{k}$ can be determined. The crystallization half-time

($t_{0.5}$), i.e., the time required for a specimen to complete half of the final crystallinity, was also determined using equation Eq. (9) to better comprehend the nucleation mechanism.

$$t_{0.5} = \left(\frac{\ln 2}{\boldsymbol{k}}\right)^{1/\boldsymbol{n}} \tag{9}$$

2.3.4. Thermogravimetric analysis

TGA analyses were performed using a TGA Q50 analyzer (TA Instruments, USA) under N_2 flow (50 mL.min^{-1}). A mass (5–20 mg) of each formulation was placed in an aluminum crucible and scanned from 20 to 600°C at four different constant heating speeds (10, 20, 30, and 40°C.min^{-1}). The TD kinetics of n-PBS and PBS-based blends were investigated using the Flynn–Wall–Ozawa (F–W–O) and Kissinger models (Sun et al., 2016; Zanatta et al., 2016).

As reported by Sun et al. (2016) and Zanatta et al. (2016), the integration of **Eq. (S7)** in the Supporting Information using empirical F–W–O approximation gives Eq. (10).

$$\log\boldsymbol{\beta} = \log\left(\frac{AE_a}{R.g(\alpha)}\right) - 2.315 - 0.4567\frac{E_a}{R}.\frac{\mathbf{1}}{\mathbf{T_m}} \tag{10}$$

where $\boldsymbol{\beta}$ represents is the heating rate in °C.s^{-1}. $\boldsymbol{A}$ is the frequency factor and α is the conversion rate. Eα (kJ.mol-1) is the apparent activation energy. T(°K) is the absolute temperature. $\boldsymbol{R}$ is the gas constant (8.314 J. mol^{-1}.K^{-1}). The E_a can be determined by the slope $-0.4567\frac{E_a}{R}$ of the straight line obtained by plotting log$\boldsymbol{\beta}$ against $\frac{1}{T_m}$.

Regarding the Kissinger model, Sun et al. (2016) and Zanatta et al. (2016) mentioned that the integration of **Eq. (S7)** in the Supporting Information yields Eq. (11).

$$\ln\left(\frac{\boldsymbol{\beta}}{\mathbf{T_m^2}}\right) = \ln\left(\frac{AR}{E_a}\right) - \frac{E_a}{R}.\frac{\mathbf{1}}{\mathbf{T_m}} \tag{11}$$

By plotting $\ln\left(\frac{\beta}{T_m^2}\right)$ against $\frac{1}{T_m}$ for different heat rates, E_α can be determined from the slope $-\frac{E_a}{R}$ of the straight line obtained.

2.3.5. Morphological analysis

The texture of the fracture facies and the filler dispersion state in the PBS-based blends were investigated using SEM analysis. The morphologies of all specimens were observed using a HITACHI SU1510 scanning electron microscope (Japan) operating at 15 kV with a working distance of 20 mm. Specimens were previously sputter-coated with a thin gold layer before observation to prevent image distortion due to charging.

3. Results and discussion

3.1. Water absorption measurements: kinetic and diffusion

Fig. 1a illustrates the WAP plotted against time (hours) for PBS-based materials. MCC-filled specimens exhibit a WAP of ~1 % after 24 h immersion, while PBS/CA shows a WAP of 0.65 %, n-PBS being the least absorbent material. All specimens ingest water very rapidly in the first immersion stage (0–12 h) and level off thereafter at a relative plateau where the WAP values for the materials remain constant as the water permeation reaches a stationary state. After 432 h of immersion, n-PBS equilibrates at a WAP of 0.8 %, whereas all other formulations continue to absorb water. On the one hand, this can be explained by the fact that the n-PBS chain backbones contain polar sites (ester functions, hydroxyl, and carboxyl end groups) where incoming water molecules (WM) can be fixed via H-bonds (Ahmad Thirmizir et al., 2011; Čîhal et al., 2018; Espert et al., 2004). On the other hand, the fracture facies of n-PBS in Fig. 1d exhibit cavities – of approximately 10 µm in size – which are filling flaws of the injected materials (Espert et al., 2004). These microdefects unwillingly appeared in the injected samples. As said earlier, the injection moulding had been thoroughly optimized to minimize the development these voids. These free volumes could have bungled the mechanism of the water diffusion by acting as capillary microvoids in the pure PBS (Petchwattana et al., 2017).

The PBS/CA blend saturates after 840 h of immersion, reaching its equilibrium point with a WAP of ~188 % higher than that for n-PBS. From Fig. 1a, it seems that the saturation begins at 500 h. The PBS/CA curve shows that from 0 h to 500 h, there is a first straight WAP jump. Afterwards, from 500 h to 840 h there is second slight straight WAP jump. The saturation threshold was determined from the point where the WAP does not vary by more than 10 % compared to the maximum WAP. The calculations show that from 840 h to 3200 h, the WAP increases by ~8 % while from 500 h to 3000 h, the WAP increases by ~14 %. This behavior can be ascribed to acetyl functions and polar hydrophilic hydroxyl groups in PBS and CA, which can fix WM through H-bondings, as reported by Espert et al., (2004)). Note that the CA macromolecules have more polar sites per repeating unit than PBS (see Fig. 1h), which can contribute to increased WAP (Boulven et al., 2019). . The PBS/CA fracture surface (Fig. 1e) also presents some micro-voids (~2 µm) into which WM can diffuse. These imperfections might increase the contact surface between PBS/CA and WM during the swelling time, leading to increased WAP. Taken together, these explanations could account for why PBS/CA absorbs more water than n-PBS.

PBS/MCC saturates after 1600 h with a WAP of ~463 % and ~96 % higher than the WAP for n-PBS and PBS/CA, respectively. This increased WAP, through H-bonding, can be attributed to the higher number of absorption microchannels due to the addition of hydrophilic MCC fibers to the hydrophobic PBS. Fig. 1f displays interfacial voids, poor adhesion between ingredients, and therefore greater porosity in PBS/MCC, which allows more WM to migrate into MCC structures. The capillary activity of these structural defects increases the contact surface between the ingredients and WM, thereby increasing the blend WAP owe to the strong H-bonding potential of WM. Note also that the MCC backbone chains have six HO – per cellobiose repeating unit while CA macromolecules have only two HO – . This high density of available polar sites explains the swelling capacity of MCC fibers, which can absorb more WM in PBS/MCC compared to all MCC-free specimens (Espert et al., 2004; Petchwattana et al., 2017). The increased WAP at higher capillary activity is generally explained by the appearance of water clusters due to WM stored in the gaps, pores, and microchannels of the composite structure (Cosquer et al., 2021; Frollini et al., 2013).

The PBS/CA/MCC hybrid shows the highest WA behavior. It gradually saturates to a plateau after 1600 h of conditioning, with a WAP of 19 % higher than that for PBS/MCC. The addition of MCC fibers appears to promote higher WAP – compared to CA – due to the high density of strong H-linking polar sites (Pang et al., 2015). However, Fig. 1a shows comparable WAP for the first immersion week (~190 h) for both MCC-filled blends. After this first stage, both materials absorb water relatively similarly until reaching equilibrium state where the WAP for PBS/CA/MCC and PBS/MCC is 550 % and ~463 % higher, respectively, than that for n-PBS. Moreover, similar to PBS/MCC, the PBS/CA/MCC fracture facies presents randomly dispersed MCC fibers. Nevertheless, contrary to MCC fibers in the inserted figure of Fig. 1f, the micrograph of the Fig. 1g show that hybrid MCC fibers are entirely whitish-coated and voids' sizes are significantly reduced. Pang and co-workers (2015) reported similar observations about cellulose acetate/kenaf fibers' biocomposites. This change of the hybrid microstructure was ascribed to the compatibilizing functionality of CA. The hybrid shows a less hollow texture with few nano-voids that serve as circulating channels for WM towards hydroxyl sites. Thus, even with higher filler content (50 wt%), the water activity in the initial hybrid specific surface is somehow restrained. Among the plausible explanations is the formation of CA interface layers around MCC fibers that would limit the WA dynamics in the first immersion stage; because all ingredients polar sites are strongly trapped within the H-bonding network as demonstrated by Sango et al. (2023). The CA layer surrounding the MCC fibers regulates and slows the WM diffusion in the MCC structure, thereby extending the hybrid

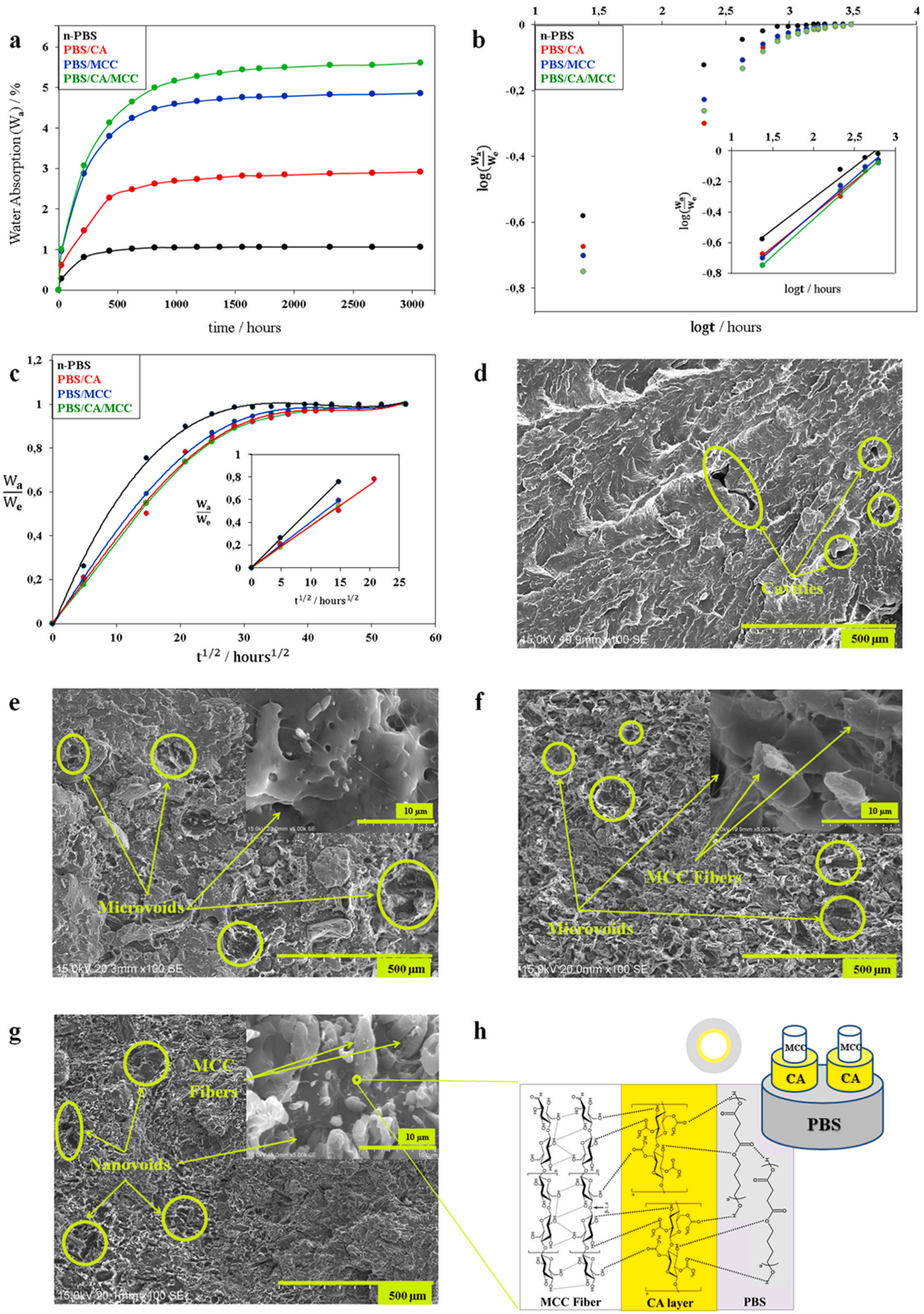

Fig. 1. (a) Plots of water absorption (W$_a$ / %) versus time (hours) for n-PBS and PBS-based blends. (b) Diffusion curve fittings for PBS-based materials. (**c**) Relationship between the WA ratio ($\frac{W_a}{W_e}$) versus $t^{1/2}$ for PBS-based materials. SEM micrographs for tensile fractured surfaces showing cavities and voids in (d) n-PBS, (e) PBS/CA, (f) PBS/MCC, and (g) PBS/CA/MCC. (h) Schematic representation of physical interactions between ingredients at the interface in the hybrid.

saturation time (Cosquer et al., 2021). In the second immersion stage, the WM previously sorbed in the first stage gradually plasticize the hybrid, which loosens the H-bonding network and frees up both hydrophilic hydroxyl and ester sites in the ingredients. These polar sites create a strong affinity with WM, which would act to increase the WAP until saturation (Espert et al., 2004; Petchwattana et al., 2017). This expansion of the effective specific surface provides available active functional sites that significantly increase the hybrid's absorption capacity. Moreover, at higher WAP, it was suggested that the coalescence of sorbed WM led to the formation of water clusters after saturation (Cosquer et al., 2021). Taken together, these arguments could account for why PBS/CA/MCC is more absorbent than PBS/MCC.

Further WA kinetic studies of the PBS-based materials were performed to plot the curves shown in Fig. 1(b-c) and determine the values of n, k, and D presented in Table 2.

For all formulations, n values are relatively close to 0.5, indicating that the swelling mechanism can be classified as Fickian (Cosquer et al., 2021). From Fig. 1a, the slope of the curve at the transient regime is clearly higher for filled materials than for n-PBS, and the water diffusion at the steady state is lower for n-PBS, indicating higher water diffusivity into the filled specimens. These results agree with previous findings (Ahmad Thirmizir et al., 2011; Petchwattana et al., 2017). The PBS/CA diffusion coefficient *D* is 20 % and 4 % lower than that for PBS/MCC and PBS/CA/MCC, respectively. This result confirms that PBS/CA hardly permeates WM more than MCC-filled formulations. Moreover, the closeness of the ***D*** values for both CA-filled materials also validates the hypothesis of the crown-like interface activity of the CA polymer around MCC fibers in the hybrid, which would restrain the diffusivity of water in the first absorption stage. Taken together, these findings suggest that, in the first conditioning week, the combination of both fillers induces an interference effect on the hybrid's WA capacity. In contrast, in the second immersion period, the WAP increases due to the synergistic activities of CA and MCC. It should be emphasized that the water absorption measurements were performed under extreme conditions: specimens were immersed in water without any side protection, which does not represent actual industrial conditions.

3.2. DSC characterization

3.2.1. Non-isothermal analysis of n-PBS and PBS-based blends

Fig. 2 exhibits the DSC thermograms obtained from the cooling of the quiescent melt of the n-PBS and the PBS-based blends.

The thermal behavior of PBS in the PBS-based materials is relatively affected when each filler is added to the biopolyester. The cooling scan of n-PBS shows an exotherm between 50°C and 90°C with a relative hot crystallization degree (χ_{hc}) of 63.73 $J.g^{-1}$ and a hot crystallization temperature (T_{hc}) of 75°C (see Table 3). These crystallization parameters significantly decrease by ~18 % and 21 %, respectively, when 20 wt% of the CA is mingled with PBS, indicating that CA chains obstructs the nucleation ability of PBS due to steric encumbrance associated with CA acetyl groups and anhydroglucosidic cycles. Several authors have reported similar conclusions (Barletta et al., 2022; Čı́hal et al., 2018; Hu et al., 2017; Shi et al., 2018; Zhou et al., 2012). Both χ_{hc} and T_{hc} increase slightly by 3 % with the addition of 30 wt% of MCC in the PBS. This confirms the light heterogeneous nucleating activity of the MCC, which induces transcrystallinity in the PBS (Hu et al., 2017; Zhang et al., 2018).

Table 2
Data for the WA mechanism from the linear fitting.

Formulations	WA at the equilibrium (%)	n	k (h^2)	D ($m^2.s^{-1}$)
n-PBS	1.0624	0.4106	0.0740	3.2154×10^{-9}
PBS/CA	2.9146	0.4358	0.0537	4.1148×10^{-9}
PBS/MCC	4.8579	0.4798	0.0443	5.0744×10^{-9}
PBS/CA/ MCC	5.6076	0.4962	0.0379	4.3687×10^{-9}

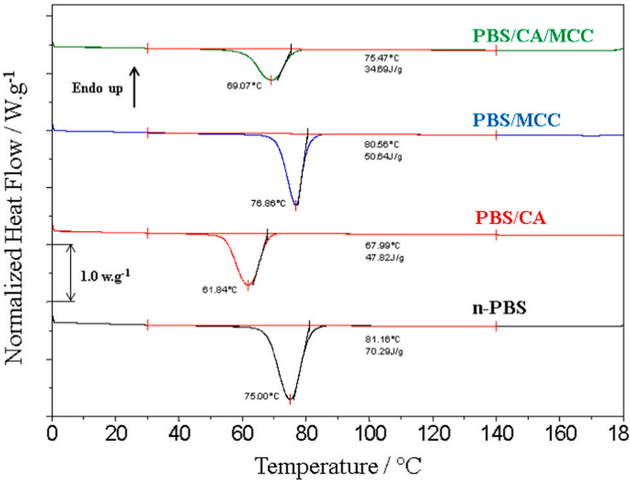

Fig. 2. Non-isothermal cooling DSC thermograms for n-PBS and PBS-based blends.

Table 3
Calorimetric data for n-PBS and PBS-based blends.

Samples	T_{hc} (°C)	ΔH_{hc} ($J.g^{-1}$)	χ_{hc} (%)
n-PBS	75* (55 – 85)	70.3±0.5	63.7±0.2
PBS/CA	62* (53 – 73)	47.8±0.3	54.2±0.6
PBS/MCC	77* (58 – 85)	50.6±0.8	65.6±0.5
PBS/CA/MCC	70* (52 – 79)	34.7±0.2	62.9±0.8

* Temperatures at the optimum of the crystallization curves

Regarding the hybrid, the combined effect of the two fillers on the structuration ability of the PBS macromolecules does not impact its relative χ_{hc}. Still, its T_{hc} decreases by 5°C compared to that of n-PBS, possibly due to H-bonds formed between the carbonyl esters and hydroxyl functions of the PBS macromolecules and CA chains resulting in intermolecular chain entanglements (Zhou et al., 2012). These entanglements would hinder the mobility of PBS chain segments, leading to weak heterogeneous nucleation efficiency of MCC fibers in the hybrid, unlike the binary PBS/MCC composite (Fig. 1h). This confirms that in the ternary hybrid, CA forms like an interface layer that coats the MCC fibers, preventing direct physical interactions between MCC and PBS. This would not be conducive to the transcrystallization in the PBS matrix. This result aligns with other relevant studies (Aliotta et al., 2022; Zhang et al., 2018).

3.2.2. Isothermal crystallization kinetics of PBS-based specimens

To understand the development of crystallinity in the hybrid during isothermal crystallization, the Avrami model was employed to compare the kinetics of PBS/CA/MCC with the other PBS-based materials. The exotherms and Avrami plots for n-PBS and the PBS-based blends are illustrated in Fig. 3. Fig. 3(a-d) show S-shaped curves for the relative crystallinity as a function of time for PBS-based materials at various temperatures. With increasing supercooling (i.e., the difference between the melting temperature and T_C), the exothermal peaks become more intense, sharper, and thinner. Consequently, the time needed to complete crystallization decreases with the isothermal crystallization temperature, regardless of the formulation. Other researchers have reviewed or reported equivalent results (Barletta et al., 2022; Frollini et al., 2013; Rafiqah et al., 2021; Vorawongsagul et al., 2021).

The Avrami plots for all formulations are illustrated in Fig. 3(m, n, p, q). The parameters n, k, and $t_{0.5}$ were calculated from the slopes and intercepts, as summarized in Table 4. Note that the crystallization

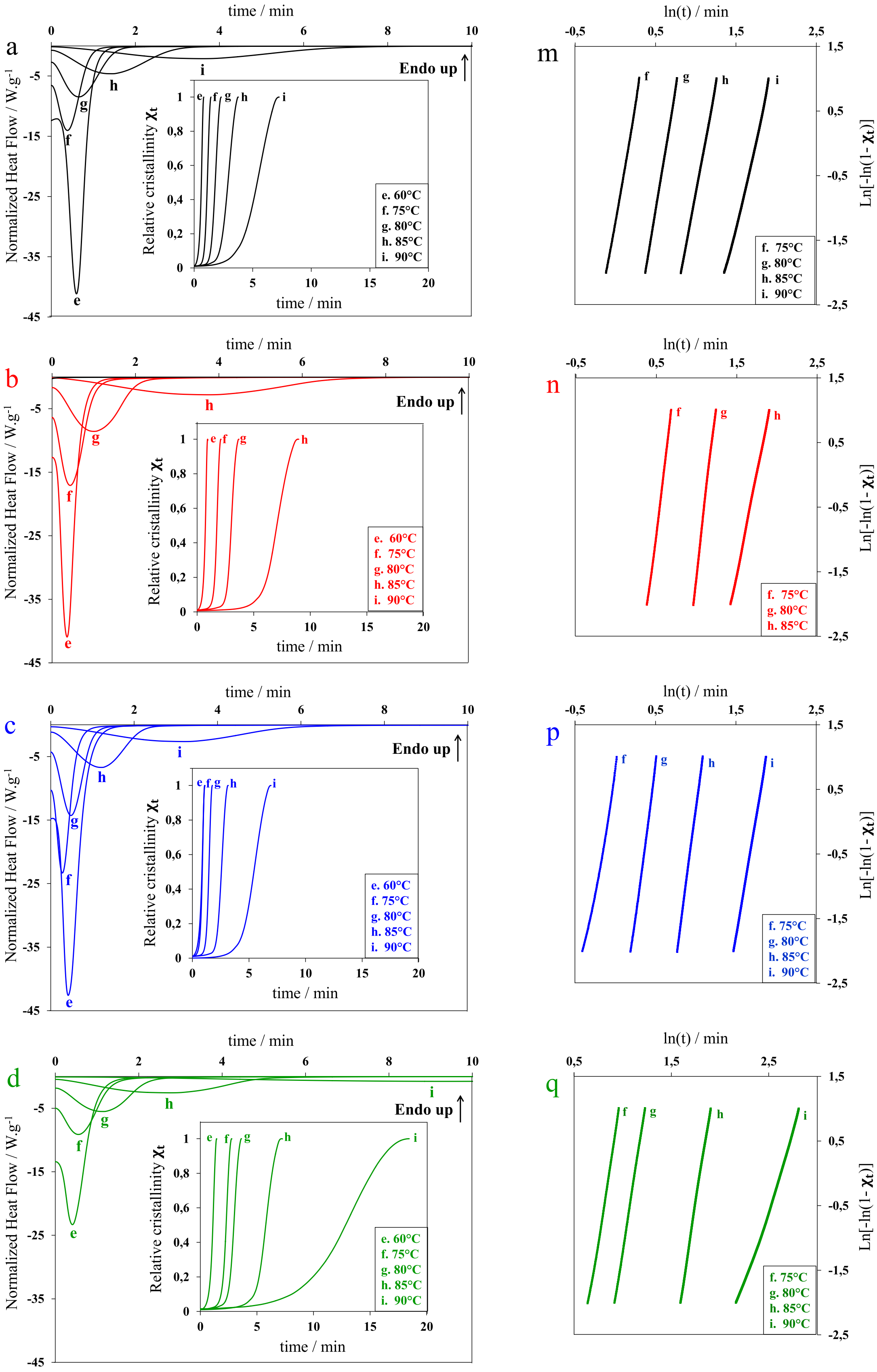

Fig. 3. Crystallization kinetics obtained from DSC thermograms for (a) n-PBS, (b) PBS/CA, (c) PBS/MCC, and (d) PBS/CA/MCC. Avrami plots of ln[−ln(1−χ_t)] against ln(t) at different isothermal crystallization temperatures: (m) n-PBS, (n) PBS/CA, (p) PBS/MCC, and (q) PBS/CA/MCC.

Table 4
DSC kinetics parameters (n, k, and $t_{0.5}$) for n-PBS and PBS-based blends.

Samples	T / °C	k min^{-1}	$t_{0.5}$ (min)	n	$n_{average}$	R^2
n-PBS						
	75	0.5304	1.13	2.19	2.46	0.985
	80	0.1747	1.81	2.33		0.988
	85	0.0412	2.89	2.66		0.991
	90	0.0037	5.38	2.64		0.999
PBS/CA	75	0.1950	1.74	2.29	2.51	0.989
	80	0.0406	3.02	2.57		0.991
	85	0.0079	5.39	2.66		0.999
	90	—	—	—		—
PBS/MCC	75	0.9984	0.87	2.62	2.76	0.984
	80	0.2406	1.45	2.83		0.987
	85	0.0454	2.56	2.90		0.986
	90	0.0076	5,43	2.67		0.998
PBS/CA/ MCC	75	0.1598	2.28	1.78	2.24	0.982
	80	0.0642	2.96	2.19		0.988
	85	0.0157	5.78	2.16		0.999
	90	0.0005	12.83	2.82		0.989

parameters for PBS significantly evolved with the addition of either or both fillers. The **n** values fluctuate between 2 and 3, regardless of the formulation, suggesting an instantaneous emergence of nucleated axialites and sporadic growth of three-dimensional truncated spherocrystals (Aliotta et al., 2022; Kuan et al., 2006; Li et al., 2017; Zhang et al., 2018). As the crystallization mechanism remains relatively unchanged for all specimens, the addition of CA and/or MCC to PBS appears to have little influence on the spatial crystal growth of PBS.

For the same T_C, the crystallization half-time ($t_{0.5}$) is shorter for n-PBS than PBS/MCC, while the $t_{0.5}$ is significantly longer for n-PBS than PBS/MCC. The $t_{0.5}$ is conventionally used to compare crystallization rates. These results are in agreement with previous non-isothermal DSC outcomes, i.e., the capacity of CA to delay crystallization and the ability of MCC fibers to accelerate the nucleation rate of polyesters (Číhal et al., 2018; Kuan et al., 2006; Li et al., 2017; Zhou et al., 2012; 2016).

The results for the $t_{0.5}$ in the ternary system seem mudding and confusing, because for the same T_C, the $t_{0.5}$ for PBS/CA/MCC and PBS/CA are quite similar. At the same time, the $t_{0.5}$ for the hybrid blend is meaningfully prolonged by over 50 % compared to n-PBS. It is worth mentioning that the evolution of the crystallization constant k corroborates the fluctuation in the $t_{0.5}$: k decreases as T_C increases, regardless of the material. For each T_C, the k values for CA-filled specimens are lower than those for n-PBS, while those for PBS/MCC are higher. Taken together, these findings strengthen the assumed crown-like interface activity of CA (see Fig. 1h) between MCC fibers and PBS in the hybrid, CA forming a co-continuous layer.

Based on the aforementioned results, there are strong physical affinities between CA chains and MCC fibers in the hybrid (see Fig. 1h): the MCC fibers appear to be enrobed by CA chains through H-bonding, while the CA macromolecules are entangled with PBS chains, restricting their molecular mobility. This wrapping weakens the nucleation ability of MCC fibers because their direct contact with PBS chains restricts the formation of spherocrystals. Zhang et al. (2018) have observed similar behavior in a ternary hybrid composite made of PLA/PBS/cellulose nanocrystals (CNCs). In that case, the CNC effect on PLA crystallization was inhibited by the addition of PBS to the hybrid. The authors justified the restriction of PLA heterogeneous nucleation by encapsulating CNCs in the PBS polymer. In the present study, the overall crystallization process (primary nucleation and superstructural crystal growth) in the hybrid appears to be influenced more by CA than MCC, indicating that the growth of heterogeneous nuclei are activated similarly in PBS/CA as well as in the PBS/CA/MCC.

3.3. Kinetics of thermal degradation for n-PBS and PBS-based blends

Fig. 4(a-f) shows the TGA-DTG thermograms for MCC, CA, n-PBS, and PBS-based blends at four heating rates (10, 20, 30, and 40°C.min^{-1}). The analysis of the TGA-DTG curves reveals that the maximum TD rate increases with increasing heating rate. Zhang and co-workers (2020) obtained similar results for wood/polycarbonate composites. The TD results for the PBS-based materials indicate only one decomposition stage for MCC-free formulations (Fig. 4(a-b)), but two decomposition stages for MCC-filled materials (Fig. 4(c-d)): the first degradation step is attributed to the pyrolysis of cellulose fibers, which occurs in the 250–480°C temperature range. In contrast, the second degradation step, which occurs between 270 and 520°C, is assigned to the pyrolysis of the PBS polymer. As the temperature increases, depolymerization reactions take place; the component polymerization degrees are reduced; cellulose anhydro-glycosidic bonds and PBS ester functions are broken; carbon-carbon bonds are cleaved; free radicals appear; H_2O, CO, and CO_2 are formed; and finally, inorganic ashes and coal are released (Mothé and de Miranda, 2013; Zhang et al., 2020).

The results for MCC-loaded materials (PBS/MCC and PBS/CA/MCC) are noteworthy: the DTG thermograms for PBS/MCC show a kind of "Russian-mountain" profile, while the PBS/CA/MCC shows a staircase-like profile, regardless of the heating rate. This indicate that there is a physical cross-linked continuity between MCC fibers, CA, and PBS in the hybrid composite: it seems that there are strong physical affinities between CA chains and MCC fibers in the hybrid due to a highly densified H-bond network, confirming that the MCC fibers are encapsulated in the CA polymer. As shown in Fig. 4(e-f), CA is more thermally stable than MCC fibers, regardless of the heating rate (Boulven et al., 2019). It seems that CA behaves like a co-continuous layer between MCC and PBS, thereby delaying the degradation of the cellulose fibers. This will be demonstrated in the following sub-sections.

To better understand the TD behavior of the hybrid, the activation energies ($\mathbf{E_a}$) for MCC, CA, n-PBS, and PBS-based blends were determined using the Kissinger and F–W–O models. The kinetic parameters determined by different approaches are comparable when calculated on similar scales (Zanatta et., 2016).

3.3.1. The Kissinger model

Fig. S1(a-b) in the Supporting Information displays the linear plots of **ln** $\left(\frac{\beta}{T_m^2}\right)$ against $\frac{1}{T_m}$ using the Kissinger method for MCC, CA, n-PBS, and PBS-based blends: **a**. First maximal degradation step (pyrolysis of the MCC fibers), **b**. Second maximal degradation step (pyrolysis of the PBS). All $\mathbf{E_a}$ values were determined from the MCC and PBS degradation peaks of the DTG curves using the maximum thermal decomposition temperature ($T_{d.max}$) for each heating rate. The calculations yielded two types of E_a for each MCC-filled specimen and one E_a for each MCC-free specimen. $E_{a,1}$ values can be correlated with the thermal degradation of MCC in the pure form and in the composites. In contrast, $E_{a,2}$ values represent the second activation energies corresponding to PBS degradation in the neat polymer and in all the blends. The E_a ($E_{a,1}$, $E_{a,2}$) values were calculated from the linear slope data, as plotted in Fig. S1(a-b) and presented in Table 5.

The second PBS activation energy ($E_{a,2}$) in for the n-PBS is lower than that for PBS in the PBS-based blends. Furthermore, if the standard deviations of the Kissinger parameter values are considered, the degradation of the PBS polymer in PBS-based materials increases with the addition of each and both fillers (MCC and CA). This is consistent with the outcomes of Zhang et al. (2020) whom have reported a similar trends. The first activation energy ($E_{a,1}$) value for MCC in PBS/MCC is slightly lower (~2 %) than that for MCC in PBS/CA/MCC. This indicates that the CA layer surrounding the fibers in the hybrid may delays the degradation of the embedded MCC phase which degrades at a higher energy, thus leading to a higher $E_{a,1}$ (107±2 kJ.mol^{-1}) value (Zanatta et al., 2016; Zhang et al., 2020). Although the Kissinger model helped to

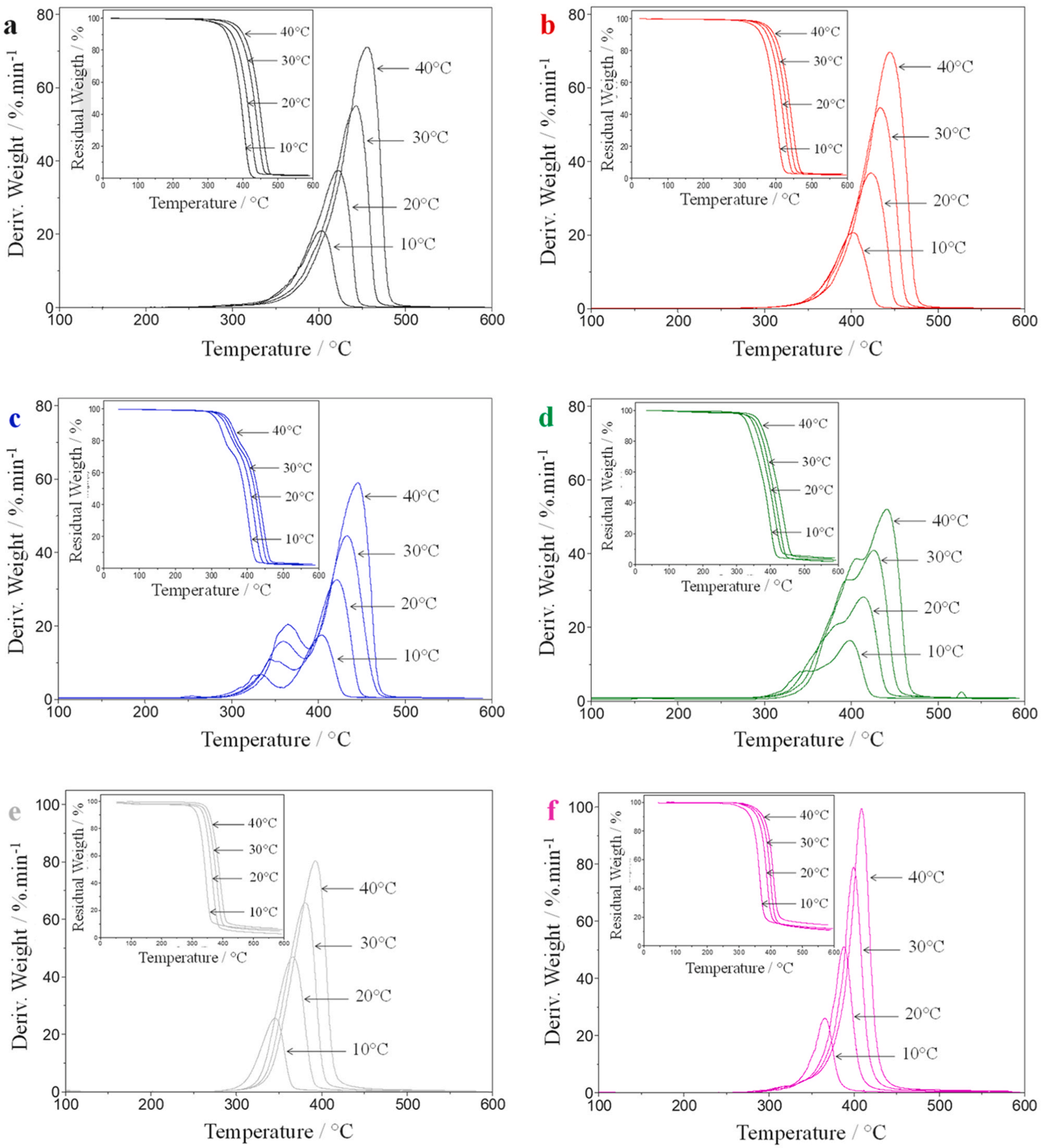

Fig. 4. TGA-DTG thermograms for (a) n-PBS, (b) PBS/CA, (c) PBS/MCC, (d) PBS/CA/MCC, (e) MCC, and (f) CA.

Table 5
Activation energy ($E_{a,1}$, $E_{a,2}$) values calculated using the Kissinger method for MCC, CA, n-PBS, and PBS-based blends.

	Kissinger method	
Samples	Ea,1 (kJ.mol–1)	Ea,2 (kJ.mol–1)
MCC	90.2 104±8	————
CA	106.8 112±7	————
n–PBS	————	94.1 98±9
PBS/CA	————	127.3 114±8
PBS/MCC	95.6 105±17	113.8 116±5
PBS/CA/MCC	64.9 107±2	115.3 118±4

understand the organization of ingredients (MCC, CA, and PBS) in the hybrid, it is important to note that this method is limited at the maximum thermal degradation temperatures of the DTG curves because, in the Kissinger model, the apparent E_a value is calculated at the point of maximum reaction rate, using different heating rates for the same conversion. Thereby, the F–W–O model is more informative because it provides reliable insights into the kinetics and mechanisms of complex reaction processes. Thus, the F–W–O model considers the evolution of the E_a with the conversion degree (α) along the entire heating domain (Sun et al., 2016).

3.3.2. The Flynn–Wall–Ozawa model

Under the F–W–O model, the E_a values were determined using the data from the isoconversional linearization slopes, as presented in Fig. S2(a-f) in the Supporting Information. The straight slopes, referring to isoconversions, show higher parallelism across the entire temperature range. The lines were plotted in the conversion rate range between α=0.1 and α=0.9, the domain where the components of the specimens decomposed. The calculated E_a values for MCC, CA, n-PBS, and PBS-based blends are reported in Fig. 5.

The thermal decomposition behavior of a multiphase material may be approximated as the sum of the contributions of its components (Mothé and de Miranda, 2013; Sun et al., 2016). Moreover, the organization of the ingredients in the material can be revealed through changes in the reaction media (Fig. 4). These changes are caused mainly by intrinsic interactions between the components at random points and heterogeneity in the materials.

Fig. 5 can be divided into two degradation sections: the transient section which is located between α=0.1 and α=0.25 corresponds to the conversion rate range where all ingredients and PBS-based materials reach the potential barrier so that the pyrolysis can start. The second section (α≥0.25) corresponds to the conversion rate range where materials are entirely degraded. The analysis of the profiles of PBS-based materials (PBS/CA, PBS/MCC, PBS/CA/MCC) shows that all their activation energies are higher than those for the ingredients (CA, MCC, PBS) taken alone. This indicates that the blending of PBS with each of both fillers (CA and MCC) generates new interactions which increase the stability of the blends.

From Fig. 5, it can be observed that CA is more stable than MCC and n-PBS in the conversion rate range between α=0.2 and α=0.9. According to Table S1 in the Supporting Information, the conversion rate of the CA polymer requires higher E_a because of the residual H-bonds and the huge volume of the acetyl groups grafted on the main skeleton. Moreover, MCC showed E_a values higher than those for n-PBS. This is ascribed to the huge density of stabilizing H-bonds present between the hydroxyl groups in the fibers. n-PBS contains very few H-bonds because the thermoplastic polymer has only two hydroxyl groups at the ends of each macromolecule. The cleavages of the carbon-carbon (C – C), the carbon-oxygen (C – O, C = O), and the cellulose anhydro-glycosidic bonds, which occurs between 300 and 470°C, is less energy-consuming in n-PBS than in MCC fibers, CA being more energy-consuming than MCC fibers. The n-PBS presents a small shoulder between α= 0.1 and α= 0.4. This is assigned to the main depolyesterification of the thermoplastic polymer chains. It is noteworthy that n-PBS and MCC activation energies drop gradually with increasing conversion rate (α ≥ 0.2) while the CA activation energies increase with the conversion rate up to α=0.7 and slightly drop afterwards. These specific behaviors are observed in polysaccharides due to their complex pyrolysis mechanism which involves multiphase reactions, highly unstable intermediate, heat, and mass transfer (Antal Jr. and Varhegyi, 1995; Lin et al., 2009).

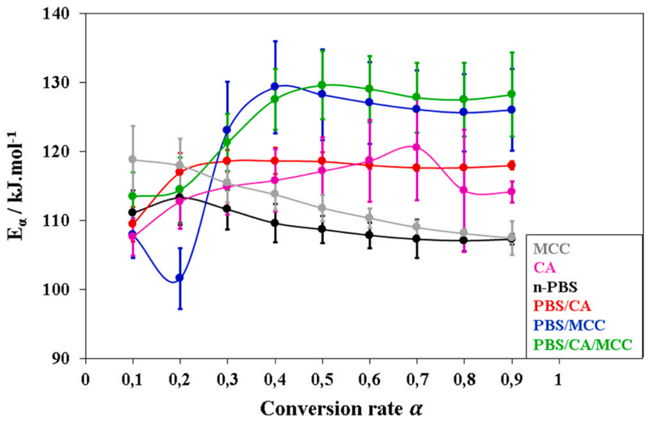

Fig. 5. Dependence of the activation energy $\mathbf{E_a}$ on the conversion rate $\boldsymbol{\alpha}$ for the thermal degradation of MCC fibers, CA, n-PBS, PBS/CA, PBS/MCC, and PBS/CA/MCC.

The analysis of PBS/CA red profile shows that its E_a values are 4 – 12 % higher than those for n-PBS in the conversion rate range between α=0.2 and α=0.9. The apparent E_a for PBS/CA jump from 109 kJ.mol^{-1} (α=0.1) to a ceiling of 124 kJ.mol^{-1} for all the conversion rates α higher than 0.28. As mentioned above, the CA activation energy increases with the conversion rate while the activation energy of n-PBS decreases from α=0.2 to α=0.9. This clearly indicates that the E_a profile for PBS/CA is highly dependent of the CA filler in the entire conversion rate range. As mentioned above, this is attributed to the miscibility between PBS and CA and the development of H-bonds and chain entanglements which stabilize the binary system. These findings agree with the results of Sango et al. (2023), where infrared spectroscopy and rheology measurements demonstrated strong physical interactions between PBS and CA via a high density of H-bondings. These new H-bonds which stabilize the binary blend are responsible for the increased PBS/CA E_a values.

The evolution of the activation energy for the PBS/MCC binary composite shows that its values drop from 108 kJ.mol^{-1} at α=0.1 to a minimum of ~102 kJ.mol^{-1} at α=0.18. This reduction of the activation energy values may be imputed to the poor interfacial adhesion between the hydrophilic MCC fibers and the hydrophobic PBS as evidenced in the Fig. 1f micrograph. This lack of interfacial continuity weakens the system and provokes the diminution of the E_a values. Afterwards, the E_a value jumps abruptly from ~102 kJ.mol^{-1} (α=0.18) up to a maximum of ~130 kJ.mol^{-1} (α=0.42) then it slightly decreases to 126 kJ.mol^{-1} at α=0.9. In the transient section, the hybrid E_a values at α=0.2 are 13 % higher than that for PBS/MCC. This confirms that the thermal degradation of MCC fibers delayed by the enrobing activity of CA. It is obvious that the synergy between MCC and CA has a positive effect on the hybrid thermal stability in the first degradation section. It was interesting to note that in the conversion rate range between α=0.46 and α=0.9, the E_a values for the PBS/CA/MCC are ~2 %, 9 %, and 20 % higher than those for PBS/MCC, PBS/CA, and n-PBS respectively. This result is in accordance with SEM observations (Fig. 1(d-g)) because, contrary to the PBS/CA blends, adding fibers to the MCC-filled PBS-based materials brings heterogeneity. Although the MCC fibers are enrobed in the CA polymer, the PBS pyrolysis in the hybrid is delayed in the second conversion rate section (α≥0.25) due to the synergistic effect of both fillers. Fortunately, it was satisfying to see that the PBS phase pyrolysis in the hybrid takes more conversion rate because it requires the highest E_a value (~130 kJ.mol^{-1}) at α=0.5 compared to the E_a value (~128 kJ.mol^{-1}) of the PBS/MCC composite. It seems that the carbon layers generated from CA and MCC degradation protect the PBS phase, thereby postponing the onset of its degradation mechanism (Barletta et al., 2022; Giri et al., 2020; Monika et al., 2019; Sun et al., 2016). This knowledge is the first step towards the development of new biobased polymer materials for thermal insulation. The exploration of hybrid PBS/CA/MCC thermal degradation in a context where CA and MCC are pre-treated with fire-retardant (boron-based or phosphorous-based) chemicals is an interesting avenue for further investigation (Zhang et al., 2020).

It is worth noting that the E_a values obtained from the F–W–O method were higher than those from the Kissinger method. This may be due to the intrinsic differences in the approximations used to develop each mathematical model (Monika et al., 2019; Wellen and Canedo, 2014; Zanatta et al., 2016).

The study proposed here showed a limitation of the nucleation activity of MCC fibers in both PBS/MCC and PBS/CA/MCC. Furthermore, the nucleation mechanism of PBS chains by encapsulated MCC fibers in the PBS/CA/MCC is very complex because the crystallization activity of the neat MCC fibers is very poor (Giri et al., 2020; Hu et al., 2017). Contrarily, cellulose whiskers (also known as cellulose nanocrystals) highly nucleate thermoplastic polymers (Azman Mohammad Taib et al., 2022; Li et al., 2017). The substitution of MCC fibers by cellulose whiskers may yield better results.

One novelty aspect of this study is that it investigates the kinetic behaviour of a cohesive ternary composite in which the components are configured in a particular way: CA was proven to behave like an active co-continuous compatibilizing agent between PBS and MCC fibers. MCC fibers were enrobed in the CA polymer. No other chemical reagent (like maleated reagents) was needed to optimize the interfacial adhesion between the ingredients.

Another finding of this work is that the enrobing activity of CA has shown a positive effect in delaying the thermal degradation of MCC fibers and in restraining the diffusivity of water molecules in its first immersion stage of the hybrid PBS/CA/MCC. This is an extreme condition that doesn't correspond to real life conditions. Generally, polymer-based materials are in contact with water molecules in the ambient humidity not in direct contact with liquid water. It can be reasonably assumed that if the hybrid is used in such reduced or moderate conditions, the enrobing activity will significantly delay the water uptake of the material.

4. Conclusions

A ternary PBS-based hybrid composite (PBS/CA/MCC) was successfully prepared via twin-screw extrusion and injection molding to investigate the influences of CA and MCC on changes in WAP, crystallization, and TD kinetics. For comparison purposes, n-PBS, PBS/CA, and PBS/MCC were prepared similarly. The results demonstrate that the synergistic and/or interference effects of CA and MCC on the PBS/CA/MCC kinetic rates strongly depend on the hybrid microstructure. The SEM micrographs of the hybrid evidenced that MCC fibers were whitish-coated by a CA layer. The coating impact was obvious in the crystallization mechanism, the thermal degradation process, and the water absorption dynamic for the hybrid. The CA encapsulation activity prevented MCC fibers from interacting directly with PBS chains in the hybrid, thereby increasing the half-crystallization time. A The CA coating activity limited the WAP in the first immersion stage. On the contrary, a synergistic effect of the combined fillers was observed in the second conditioning phase of the water absorption process due to the high plasticization effect of water molecules. The enrobing activity of CA around MCC particles helped to delay the TD of both fibers and PBS polymer as proven by the E_a values obtained from the Kissinger and the F–W–O models. Overall, this study provides comprehensive, well-mastered data to support the management and optimization of industrial processes involving ternary cellulose-based hybrid composites exposed to humidity or heat.

CRediT authorship contribution statement

Nathalie Leblanc: Writing – review & editing, Supervision. **Martin Claude Ngueho Yemele:** Writing – review & editing, Supervision. **Mohamed Ragoubi:** Writing – review & editing, Supervision. **Ahmed Koubaa:** Writing – review & editing, Supervision, Resources, Project administration, Funding acquisition. **Thomas Sango:** Writing – original draft, Methodology, Formal analysis, Data curation, Conceptualization.

Declaration of Competing Interest

The authors declare that they have no known competing financial interests or personal relationships that could have appeared to influence the work reported in this paper.

Data availability

Data will be made available on request.

Acknowledgments

The authors are deeply thankful to the Canada Research Chairs Program, the Natural Sciences and Engineering Research Council of Canada (NSERC), the Mathematics of Information Technology and Complex Systems (MITACS), and the Consortium de Recherche et d'Innovations en Bioprocédés Industriels au Québec (CRIBIQ) for the financial Support. The technical support of Mr. W. Belhadef for equipment maintenance is also gratefully acknowledged. The authors thank Mrs. M. McKyes (certified translator) for her valuable contribution in editing the English language of the present copy.

Appendix A. Supporting information

Supplementary data associated with this article can be found in the online version at doi:10.1016/j.indcrop.2024.119572.

References

Ahmad Thirmizir, M.Z., Mohd Ishak, Z.A., Mat Taib, R., Sudin, R., Leong, Y.W., 2011. Mechanical, water absorption and dimensional stability studies of kenaf bast fibre-filled poly(butylene succinate) composites. Polym. -Plast. Technol. Eng. 50 (4), 339–348.

Aliotta, L., Seggiani, M., Lazzeri, A., Gigante, V., Cinelli, P., 2022. A brief review of poly (butylene succinate) (PBS) and its main copolymers: synthesis, blends, composites, biodegradability, and applications. Polymers 14 (844), 1–23.

Antal, Jr, M.J., Varhegyi, G., 1995. Review – Cellulose pyrolysis kinetics: the current state of knowledge. Ind. Eng. Chem. Res. 34, 703–717.

Azman Mohammad Taib, M.N., Hamidon, T.S., Garba, Z.N., Trache, D., Uyama, H., Hussin, M.H., 2022. Recent progress in cellulose-based composites towards flame retardancy applications. Polymer 244, 124677.

Barletta, M., Aversa, C., Ayyoob, M., Gisario, A., Hamad, K., Mehrpouya, M., Vahabi, H., 2022. Poly(butylene Succinate) (PBS): materials, processing, and industrial applications. Prog. Polym. Sci. 132 (101579), 1–62.

Boulven, M., Quintard, G., Cottaz, A., Joly, C., Charlot, A., Fleury, E., 2019. Homogeneous acylation of cellulose diacetate: towards bioplastics with tuneable thermal and water transport properties. Carbohyd. Polym. 206, 674–684.

Číhal, P., Vopička, O., Lanč, M., Kludský, M., Velas, J., Hrdlička, Z., Michalcová, A., Dendisová, M., Friess, K., 2018. Poly(butylene succinate)-cellulose triacetate blends: permeation, pervaporation, sorption and physical structure. Polym. Test. 65, 468–479.

Cosquer, R., Pruvost, S., Gouanvé, F., 2021. Improvement of barrier properties of biodegradable polybutylene succinate/graphene nanoplatelets nanocomposites prepared by melt process. Membranes 11 (151), 1–25.

Espert, A., Vilaplana, F., Karlsson, S., 2004. Comparison of water absorption in natural cellulosic fibres from wood and one-year crops in polypropylene composites and its influence on their mechanical properties. Compos. Part A 35, 1267–1276.

Frollini, E., Bartolucci, N., Sisti, L., Celli, A., 2013. Poly(butylene succinate) reinforced with different lignocellulosic fibers. Ind. Crops Prod. 45, 160–169.

Giri, J., Lach, R., Le, H.H., Grellmann, W., Saiter, J.-M., Henning, S., Radusch, H.-J., Adhikari, R., 2020. Structural, thermal and mechanical properties of composites of poly(butylene adipate-co-terephthalate) with wheat straw microcrystalline cellulose. Polym. Bul. 78, 4779–4795.

Hu, X., Su, T., Pan, W., Li, P., Wang, Z., 2017. Difference in solid-state properties and enzymatic degradation of three kinds of poly(butylene succinate)/cellulose blends. RSC Adv. 7 (56), 35496–35503.

Huang, F., Wu, X., Yu, Y., Lu, Y., Chen, Q., 2017. Acylation of cellulose nanocrystals with acids/trifluoroacetic anhydride and properties of films from esters of CNCs. Carbohyd. Polym. 155, 525–534.

Ku, H., Wang, H., Pattarachaiyakoop, N., Trada, M., 2011. A review on the tensile properties of natural fiber reinforced polymer composites. Compos.: Part B 42 (4), 856–873.

Kuan, C.-F., Ma, C.-C.M., Kuan, H.-C., Wu, H.-L., Liao, Y.-M., 2006. Preparation and characterization of the novel water-crosslinked cellulose reinforced poly(butylene succinate) composites. Comp. Sci. Technol. 66 (13), 2231–2241.

Li, Y.-D., Fu, Q.-Q., Wang, M., Zeng, J.-B., 2017. Morphology, crystallization and rheological behavior in poly(butylene succinate)/cellulose nanocrystal nanocomposites fabricated by solution coagulation. Carbohyd. Polym. 164, 75–82.

Lin, Y.–C., Cho, J., Tompsett, G.A., Westmoreland, P.R., Huber, G.W., 2009. Kinetics and mechanism of cellulose pyrolysis. J. Phys. Chem. C. 113 (46), 20097–20107.

Monika, A.K.P., Mulchandani, N., Katiyar, V., 2019. Generalized kinetics for thermal degradation and melt rheology for poly(lactic acid)/poly(butylene succinate)/functionalized chitosan based reactive nanobiocomposite. Int. J. Biol. Macromol. 141, 831–842.

Mothé, C.G., de Miranda, I.C., 2013. Study of kinetic parameters of thermal decomposition of bagasse and sugarcane straw using Friedman and Ozawa–Flynn–Wall isoconversional methods. J. Therm. Anal. Calor. 113, 497–505.

Pang, C., Shanks, R.A., Daver, F., 2015. Characterization of kenaf fiber composites prepared with tributyl citrate plasticized cellulose acetate. Compos.: Part A 70, 52–58.

Petchwattana, N., Sanetuntikul, J., Sriromreun, P., Narupai, B., 2017. Wood plastic composites prepared from biodegradable poly(butylene succinate) and Burma Padauk sawdust (*Pterocarpus macrocarpus*): water absorption kinetics and sunlight exposure investigations. J. Bionic Eng. 14 (4), 781–790.

Platnieks, O., Gaidukovs, S., Thakur, V.K., Barkane, A., Beluns, S., 2021a. Bio-based poly (butylene succinate): recent progress, challenges and future opportunities. Eur. Polym. J. 161 (110855), 1–24.

Platnieks, O., Sereda, A., Gaidukovs, S., Thakur, V.K., Barkane, A., Gaidukova, G., Filipova, I., Ogurcovs, A., Fridrihsone, V., 2021b. Adding value to poly(butylene succinate) and nanofibrillated cellulose-based sustainable nanocomposites by applying masterbatch process. Ind. Crops Prod. 169 (113669), 1–12, 2021b.

Quintana, R., Persenaire, O., Lemmouchi, Y., Sampson, J., Martin, S., Bonnaud, L., Dubois, P., 2013. Enhancement of cellulose acetate degradation under accelerated weathering by plasticization with eco-friendly plasticizers. Polym. Degrad. Stab. 98, 1556–1562.

Rafiqah, S.A., Khalina, A., Harmaen, A.S., Tawakkal, I.A., Zaman, K., Asim, M., Nurrazi, M.N., Lee, C.H., 2021. A review on properties and application of bio-Based Poly(butylene succinate). Polymers 13, 1436, 1–28.

Sango, T., Koubaa, A., Ragoubi, M., Ngueho Yemele, M.C., Leblanc, N., 2023. Activities of cellulose acetate and microcrystalline cellulose on the thermal and morphomechanical performances of a biobased hybrid composite made polybutylene succinate. Int. J. Biol. Macromol. 253, 126918.

Shi, K., Liu, Y., Hu, X., Su, T., Li, P., Wang, Z., 2018. Preparation, characterization, and biodegradation of poly(butylene succinate)/cellulose triacetate blends. Int. J. Biol. Macromol. 114, 373–380.

Sun, L., Wu, Q., Xie, Y., Song, K., Lee, S., Wang, Q., 2016. Thermal decomposition of fire-retarded wood flour/polypropylene composites. J. Therm. Anal. Calorim. 123, 309–318.

Vorawongsagul, S., Pratumpong, P., Pechyen, C., 2021. Preparation and foaming behavior of poly(lactic acid)/poly(butylene succinate)/cellulose fiber composite for hot cups packaging application. Food Pack. Shelf Life. 27 (100608), 1–8.

Wellen, R.M.R., Canedo, E.L., 2014. On the Kissinger equation and the estimate of activation energies for non-isothermal cold crystallization of PET. Polym. Test. 40, 33–38.

Zanatta, E.R., Reinehr, T.O., Awadallak, J.A., Kleinübing, S.J., dos Santos, J.B.O., Bariccatti, R.A., Arroyo, P.A., da Silva, E.A., 2016. Kinetic studies of thermal decomposition of sugarcane bagasse and cassava bagasse. J. Therm. Anal. Calorim. 125 (1), 437–445.

Zhang, J., Koubaa, A., Xing, D., Liu, W., Wang, H., Wang, X.M., Wang, Q., 2020. High-performance lignocellulose/polycarbonate biocomposites fabricated by in situ reaction: structure and properties. Compos. Part A 138 (106068), 1–2.

Zhang, X., Shi, J., Ye, H., Dong, Y., Zhou, Q., 2018. Combined effect of cellulose nanocrystals and poly(butylene succinate) on poly(lactic acid) crystallization: the role of interfacial affinity. Carbohyd. Polym. 179, 79–85.

Zhang, Q., Song, M., Xu, Y., Wang, W., Wang, Z., Zhang, L., 2021. Bio-based polyesters: recent progress and future prospects. Prog. Polym. Sci. 120 (101430), 1–42.

Zhang, X., Wang, X., 2018. Polybutylene succinate/cellulose nanocrystals: role of phthalic anhydride in squeeze oriented bionanocomposites. Carbohyd. Polym. 196, 254–261.

Zhou, M., Fan, M., Zhao, Y., Jin, T., Fu, Q., 2016. Effect of stretching on the mechanical properties in melt-spun poly(butylene succinate)/microfibrillated cellulose (MFC) nanocomposites. Carbohyd. Polym. 140, 383–392.

Zhou, W., Yuan, S., Chen, Y., Bao, L., 2012. Morphology and hydrogen-bond restricted crystallization of poly(butylene succinate)/cellulose diacetate blends. J. Appl. Polym. Sci. 124, 3124–3131.